Contributions to Mineralogy and Petrology (2022) 177:41
https://doi.org/10.1007/s00410-022-01909-6

ORIGINAL PAPER

Early magmatic history of the IBM arc inferred from volcanic minerals and melt inclusions from early–late Oligocene DSDP Site 296: a mineral–melt partition approach

Eshita Samajpati[1] · **Rosemary Hickey-Vargas**[1]

Received: 12 January 2021 / Accepted: 14 March 2022 / Published online: 21 March 2022

Abstract

The magmatic history of the early Izu-Bonin-Mariana (IBM) arc forms a gap between a growing understanding of Eocene subduction and IBM arc initiation in the western Pacific, and Miocene- recent IBM arc processes. Fresh volcanic minerals in lapilli tuffs drilled at DSDP Site 296 on the northern Kyushu Palau Ridge (KPR) provide an opportunity to understand the early–late Oligocene magmatic evolution of the IBM arc leading up to arc rifting and opening of the Shikoku back-arc basin. In this study, we use major and trace element compositions of feldspar, amphibole and pyroxene, with melt inclusions, to infer KPR magma compositions, crystallization temperatures and pressures, and temporal sequence. A major finding of this approach is that inferred magma compositions span a wider range of trace element variation than that inferred from basaltic to dacitic glass shards within the tuffs. Elemental and thermobarometric data for clinopyroxene indicate the presence of mafic, incompatible element-depleted ($Nb/Yb < 0.3$ and $La/Sm_N < 1.4$) magmas that crystallized at shallow depths, and incompatible element-enriched ($Nb/Yb = 8.1$ and $La/Sm_N = 6.5$), mafic, amphibole-bearing arc magmas that either crystallized over a range of pressures or without reaching plagioclase saturation. We interpret the incompatible element-depleted magmas as decompression melts of a shallow BABB source mantle and the incompatible element-enriched type as mature, water-rich arc magmas. The occurrence of both types of magma in several lapilli tuff intervals in the drilled section suggests that arc extension and rifting was a gradual process leading to multiple events of decompression melting interspersed with the eruption of mature arc magma.

Keywords DSDP Site 296 · IBM arc · Clinopyroxene · Amphibole · Volcaniclastic sediment

Introduction

The Izu-Bonin Mariana arc (Fig. 1a) in the Western Pacific is well recognized as an ideal location to study and understand arc evolution (Stern et al. 2003). Periodic rifting of the arc since subduction initiation in the Eocene has formed a series of inactive remnant arcs and intervening basins, each providing a window to early IBM history. Initiation of the IBM arc at about 52 Ma (Fig. 1a) may have occurred when lithospheric subsidence began along a preexisting oceanic transform margin or fracture zone (Reagan et al. 2019), or, alternatively, as result of an extension event which separated the Amami Plateau, Oki-Daito and Daito Ridges (Fig. 1a), reducing upper plate strength, and allowing lower plate subsidence (Leng and Gurnis 2015). In either case, shortly after subduction initiation, seafloor spreading resulted in the rapid formation of fore-arc basalts or FABs along the entire length of the IBM system followed by the eruption of boninites, generated by shallow level melting of the mantle with the addition of water-rich fluids released from the subducting plate (Stern et al. 1991; Taylor et al. 1994; Reagan et al. 2010, 2019; Ishizuka et al. 2011a; Arculus et al. 2015a, b; Maunder et al. 2020). After 5 Ma, there was a transition from subsidence to true subduction and the first or early (Oligocene) magmatic arc was established with eruption of geochemically typical arc magma types (Stern et al. 2003; Brandl et al. 2017; Hamada et al. 2020; Ishizuka et al. 2020). In the late Oligocene, arc volcanism was disrupted by rifting

Communicated by Timothy L. Grove.

✉ Eshita Samajpati
eshitasamajpati@gmail.com

[1] Department of Earth and Environment, Florida International University, 11200 SW 8th St, PC 340, Miami, FL 33199, USA

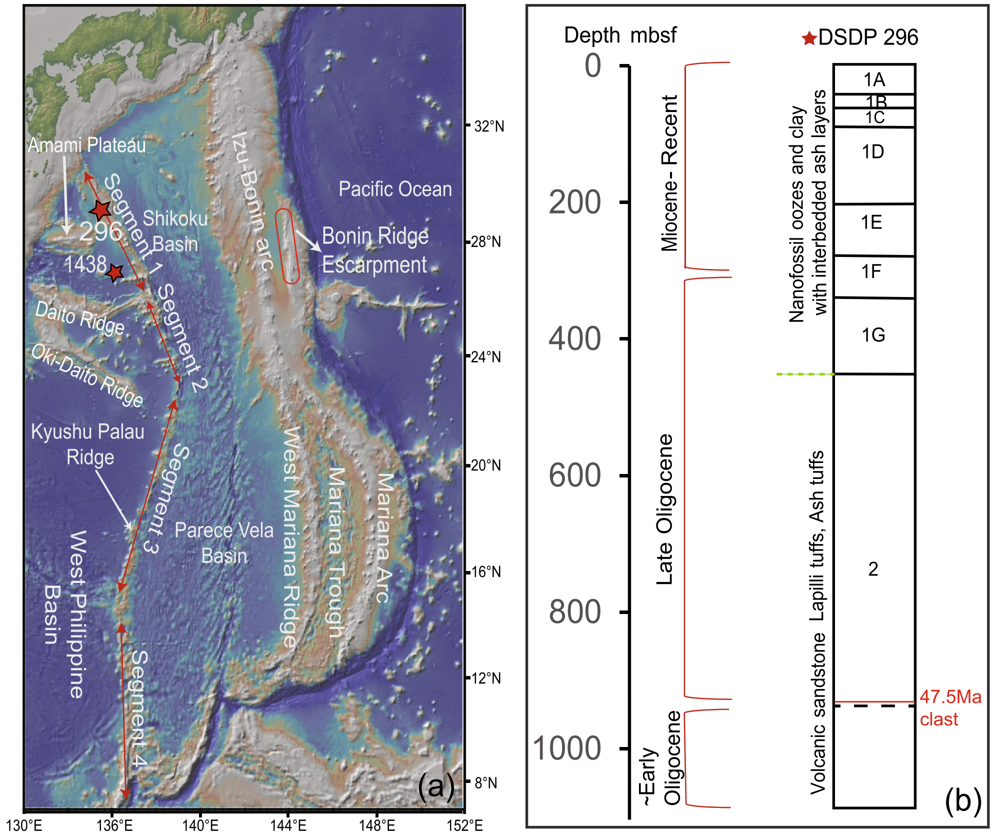

Fig. 1 **a** Map of the present day Izu-Bonin Mariana arc and features of the Philippine Sea plate made using GeoMapApp (www.geomapapp.org; Ryan et al. 2009). The Kyushu Palau ridge has been divided into four segments as per Ishizuka et al. (2011b). Red stars shows the location of DSDP Site 296 and IODP Site U1438. **b** Litho-stratigraphic sequence as defined by the Shipboard Party, DSDP Leg 31 (Ingle et al. 1975)

and opening of the Parece Vela in the south and Shikoku basin in the north, separating the Kyushu Palau Ridge from the then active IBM Arc (Karig 1975; Taylor et al. 1992; Okino et al. 1994; Kobayashi et al. 1995; Ishizuka et al. 2011a). After a period of back arc basin opening by seafloor spreading, volcanism along the arc front resumed around 17 Ma and continued until 7 Ma, when another period of back arc basin formation in the south formed the remnant West Mariana Ridge and Mariana Trough (Yamazaki and Stern 1997). The presently active (5–0 Ma) Izu-Bonin-Mariana arc has been studied in detail for several decades (Arculus et al. 1992; Stern et al. 1993, 2003; Lee et al. 1995; Elliot et al. 1997; Hochstaedter et al. 2001; Pearce et al. 2005).

Compared to the active IBM, understanding of early arc evolution is still developing, with a shift in focus of IBM studies to remnant arcs such as the Kyushu Palau Ridge (KPR) and forearc and reararc exposures of the early arc and arc initiation sequences (e.g., Arculus et al. 2015a, b; Reagan et al. 2019; Ishizuka et al. 2020). To date, most studies of the Oligocene (early) IBM arc have been based on dredged volcanic and plutonic rocks, and glass, mineral, and melt inclusions from sites drilled in the back arc and forearc regions (Lee et al. 1995; Haraguchi et al. 2003, 2012; Straub 2003, 2008; Savov et al. 2006; D'Antonio et al. 2006; Ishizuka et al. 2011b; Arculus et al. 2015b; Brandl et al. 2017; Hamada et al. 2020; Samajpati and Hickey-Vargas 2020; Ishizuka et al. 2020), leading to a developing, but incomplete, understanding of spatial and temporal variations. One advance in this direction is the comprehensive survey of volcanic rocks recovered by dredging and piston core (5–10 m depth) on the crest of the KPR by Ishizuka et al. (2011b) which defined four along-arc chemical segments of the early IBM arc (Fig. 1a).

In this study, we focus on the early to late Oligocene section of detrital and tuffaceous sediments cored at DSDP Site 296 in the northernmost KPR (Fig. 1). We use major and trace element chemistry of orthopyroxene (opx), clinopyroxene (cpx), amphibole (amph), feldspar and melt inclusions (MI) within pyroxene to model the major and trace element composition of the melts in equilibrium with them and their pressure and temperature of origin. We then compare these compositions with those of detrital glass shards from the same section (Samajpati and Hickey-Vargas 2020) to extend our understanding of IBM arc magma chemistry in this location in the Oligocene. Since Site 296 is located in the northernmost section of the KPR (Fig. 1a), within geochemical Segment 1 of Ishizuka et al. (2011b), we compare our results with published data for other locations within Segment 1 to interpret magmatic evolution without the potential impact of along-arc variation. The unique aspects of this work are: (1) emphasis on the late Oligocene, pre- to post-rifting stage of IBM arc evolution; (2) the inference of major and trace element magma compositions from minerals, using thermometry and compositionally matched partition coefficients; and (3) the opportunity to compare results inferred from mineral chemistry with geochemical data for melt inclusions and detrital glass shards from the same site in interpreting magma evolution.

Methods

Core samples

Deep Sea Drilling Project Leg 31 Site 296 was located in a graben like structure in the northernmost Kyushu Palau Ridge, and consists of two distinct lithological Units, 1 and 2 (Fig. 1b). Unit 1 comprises 453 m of clayey nannofossil chalks and oozes of late Oligocene to late Pleistocene/Holocene age with interbedded layers of volcanic ash. The base of Unit 1 coincides in time with the subsidence of the arc following rifting and opening of the Shikoku basin (Ingle et al. 1975). The underlying Unit 2 comprises 634 m of early to late Oligocene interbedded tuffs, lapilli tuffs and volcanic sandstones derived from the active Oligocene KPR arc. Ages of cores 34 through 63 (310–975.5 m) were well constrained to be late Oligocene, based on calcareous nannofossil and foraminifera biostratigraphy (Ingle et al. 1975). Ages for basal cores 64 and 65 (1070.5–1087 m) were less well constrained due to sparse nannofossil recovery and could be early Oligocene or older. Leg 31 scientists interpreted the tuffs as direct deposits from volcanic eruptions and the volcanic sandstones as the products of the erosion and deposition of sediment from ridges around Site 296. Only minerals extracted from the tuffs correspond in age with their biostratigraphic age, while sandstones may contain older material.

The tuffs and lapilli tuffs of Unit 2 consist of angular and poorly sorted lithic fragments, glass shards, and volcanic minerals such as plagioclase, pyroxenes, and titano-magnetite with a sparse amount of amphibole, in a matrix of palagonitized glass. According to the Shipboard Party, cores 52, 54, 56 and 57 are most likely to be ash-fall accumulations. Volcanic sandstones are more abundant below 750 m and are composed of the same materials as the tuffs, but rounded and sorted (Ingle et al. 1975; this study).

Mineral grains for analysis were picked from intervals of tuff and lapilli tuff as discussed below. The feldspar grains picked were usually clear and white without any signs of alteration. Clinopyroxenes were typically in shades of green or black, whereas orthopyroxenes were orange and brown. Both had inclusions of oxide, feldspar, and melt inclusions. Amphiboles were present as black grains slightly more opaque than the pyroxene grains under a binocular microscope. The amphiboles had inclusions of feldspar, oxide, and apatite; melt inclusions were mostly absent.

Analytical technique

Twenty-two core intervals selected for their coarse grain size and fresh appearing mineral grains were disaggregated in deionized water; 21 from Unit 2 (lapilli and ash tuffs) and one from the base of Unit 1G (clay-rich nannofossil chalk with volcanic ash). The resulting sediment was sieved, rinsed, and handpicked at 500-μm to 1-mm grain size. Minerals were first identified under a binocular microscope and later using Scanning Electron Microscopy with Energy Dispersive X-ray Spectroscopy (SEM–EDS). The grains were then mounted in epoxy, polished, and carbon-coated for Electron Probe Microanalysis (EPMA). Melt inclusions inside the pyroxenes were first identified using backscattered electron imaging and then analyzed for major oxides. Melt inclusions (MIs) that were round and intact and did not show evidence of post entrapment crystallization were analyzed. Large MIs were rare; the size of the melt inclusions analyzed was typically 30–60 μm. Major oxides of the minerals and melt inclusions were analyzed using a JEOL 8900 Superprobe EPMA at the Florida Center for Analytical Electron Microscopy at Florida International University (FIU). Reference materials (Enstatite, Diopside, Kaersutite and BHVO-2 glass) were analyzed before and after each sample to check the accuracy of the analysis. The analysis was done using a 1 μm beam for minerals, 2.5 μm for MIs, at 20 nA current, and 15 kV with two spots analyzed per grain. For Na and K, the beam was defocused during analysis to minimize volatilization. For feldspars and pyroxenes, the grains yielding totals in the range of 99–101 wt% are reported. For melt inclusions, totals were as low as 90% for felsic compositions. The amphiboles analyzed had totals between 94 and 98%.

Trace elements in the amphiboles, pyroxenes and melt inclusions, were analyzed by Laser Ablation ICP-MS using the Elan 6100 ICP-MS at the Trace Evidence Analysis Facility at FIU, using a New Wave 213 nm laser. NIST 612 was used as the calibrator and BHVO-2 glass as the external reference material. Spot size for minerals was 80 μm, and for melt inclusions, it was 40–55 μm, with a 10 Hz laser repetition rate and 100% output for both. The size of the inclusions did not allow for more than one spot, and inclusions smaller than 40 μm were not analyzed. Integration intervals for the data signal of samples was selected using the software Glitter (Griffin et al. 2008), with ^{40}Ca as the internal standard previously analyzed by EPMA.

Smear slides were prepared for all the samples to compare mineral abundances in the coarse and finer sediments. The size of the grains used for making smear slides was between 75 and 100 µm. Data for all analyses and accuracy and precision for standard analysis can be found in the supplementary files (Online Resource 1–5,7).

Results

Feldspars

Feldspar grains had occasional melt inclusions and mineral inclusions of titano-magnetite, pyroxene, and apatite. Compositionally, all the feldspars analyzed were plagioclase with a bimodal distribution centered around Anorthite (An) content of $An_{45\text{-}60}$ and $An_{85\text{-}95}$, although intermediate varieties were also observed (Fig. 2). Among the plagioclase analyzed, Andesine (38%) is the most common type followed by Bytownite (23%), Labradorite (21%), and Anorthite (18%) (Fig. 2). The K_2O content of the plagioclases is consistently < 0.6%, MgO and FeO contents are less than 0.1% and 1%, respectively, although few Bytownites have slightly higher MgO (0.2–0.8 wt%) and FeO (2.3–4.7 wt%) contents. The bimodal variation is observed throughout the core, but anorthite-rich plagioclase becomes more dominant towards the top of Unit 2 (Fig. 2).

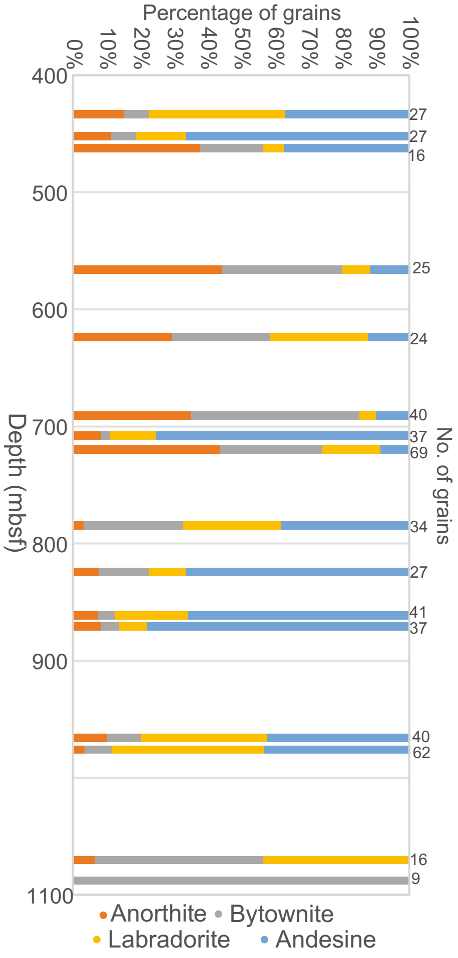

Fig. 2 Depth vs. cumulative frequency of compositional range of plagioclase at different depths

Pyroxenes

Both clinopyroxenes (cpx) and orthopyroxenes (opx) are present in Unit 2, however, the presence of orthopyroxene is low in the core intervals studied and absent in a few (Online Resource 3). Compositionally, opx are Bronzite-Hypersthene with a composition of $En_{54\text{-}73}Wo_{2\text{-}4}$ (Fig. 3a). No highly magnesian enstatite or clinoenstatite, usually associated with boninites, was identified. Mg numbers (Mg# = (cation Mg)*100/(cation Mg + cation Fe)) of the opx are between 56 and 77. Cpx falls mainly in the diopside and augite field (Fig. 3a), with compositions of $Wo_{36\text{-}48}En_{36\text{-}50}$ and Mg# ranging from 61 to 92.

Primitive Mantle (PM) normalized trace element patterns of all cpx show Nb depletion compared with LREE (light rare earth elements) and LILE (large ion lithophile elements). Clinopyroxenes show LREE depletion compared to middle REE (MREE) and heavy REE (HREE), and Zr, Hf, and Th depletion compared to LREE (Fig. 3b). Higher concentrations of incompatible trace elements are observed in low Mg# grains and vice versa (Fig. 3b). Most high-Mg# cpx have very low concentrations of LREE and other trace elements, sometimes close to the detection limit.

Amphibole

Amphibole is not a common mineral in the lapilli and ash tuffs, but amphiboles in the size range 500–1000 µm are present in the upper part of Unit 2 from cores 49 to 57 at depths of 453–719 m below sea sea floor (mbsf). Smear slides of sediments from deeper intervals (cores 59–65) using the 75–100 µm size fraction are also amphibole-free except for core 60R-1 W, 8–11 cm. Compositionally all amphiboles are calcic amphiboles (Fig. 4a), and can be subdivided into magnesiohornblende, edenite, and magnesiohastingsites using the Leake et al. (1997) classification scheme. The Mg#s of the amphiboles range from 57 to 73. The PM normalized trace element concentrations show depletion of Th and Nb relative to LREEs and depletion of Zr and Hf relative to REEs (Fig. 4b). From the trace element plot, there are two distinct groups of amphiboles, with some

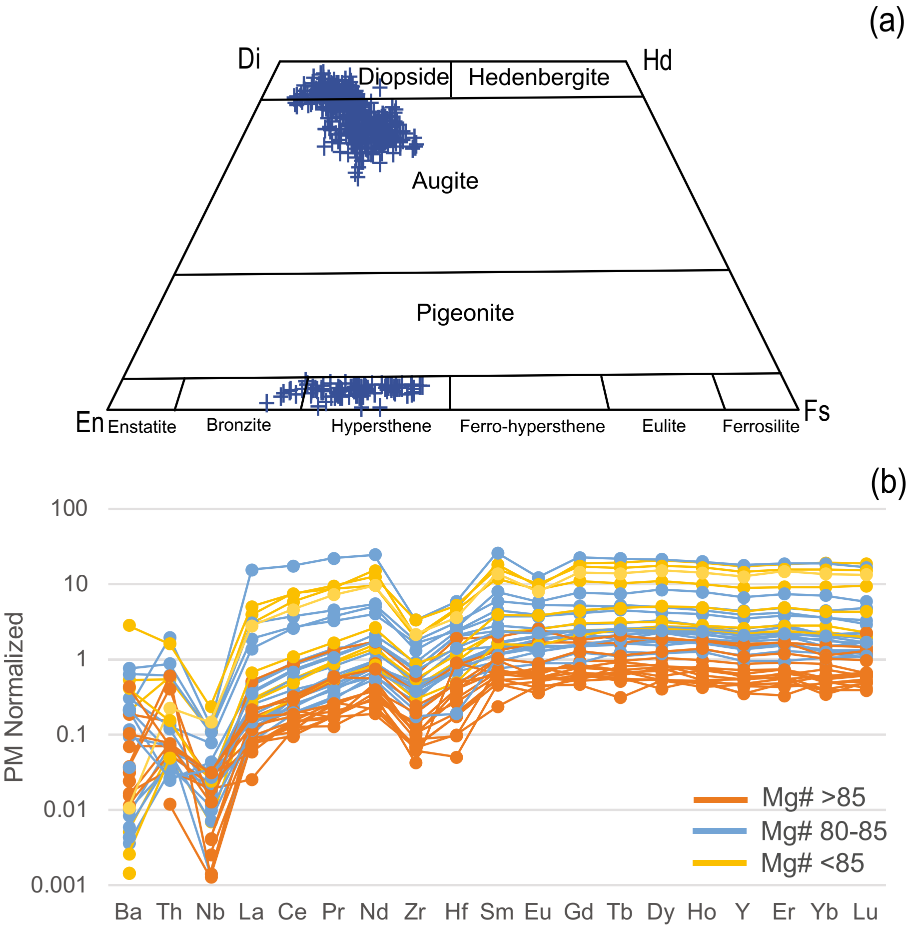

Fig. 3 **a** Plot showing the composition of pyroxenes at Site 296 on the pyroxene quadrilateral. **b** Primitive mantle normalized multi-elemental composition of some mafic clinopyroxenes. Normalizing values are from Sun and McDonough (1989)

intermediates. One group is slightly depleted in LREE and HREE and shows enrichment of Ti compared to MREE and no Eu depletion. The other group is enriched in LREE compared to MREE, depleted in Eu and Ti, and has flat MREE and HREE (Fig. 4b).

Melt inclusions

Melt inclusions within pyroxene are typically between 10 and 60-µm in size and are found in both orthopyroxenes and clinopyroxenes; only the largest ones were analyzed. Some pyroxene grains had more than one melt inclusion; when analyzed, they had similar major oxide compositions (Online Resource 5). SiO_2 contents range from 47 to 73 wt%, while the Mg#s of most basaltic MIs (48 to 52 wt% SiO_2) range from 39 to 53. The total oxide composition for most of the felsic and some intermediate MIs are as low as 90 wt% whereas, mafic ones are about 95 wt% or higher, which might reflect higher volatile contents of felsic inclusions. Without normalization, all the MIs plot within the medium K series on a plot of K_2O vs SiO_2 after the classification scheme of Peccerillo and Taylor (1976), similar to glass shards from Unit 2 (Samajpati and Hickey-Vargas 2020) (Fig. 5a). Overall, there is Mg–Fe disequilibrium between most MIs and host cpx, as the $Kd_{Fe\text{–}Mg}$ (Putirka et al. 2008) for the pairs are below the equilibrium line (Fig. 5b). The disequilibrium suggests that there were post-entrapment chemical exchanges between the MIs and the host mineral. Normalized trace element patterns show depleted to highly enriched LREE/MREE (La/Sm_N 0.33 to 4.03) and subduction-related geochemical signatures like Nb and Ta depletion relative to LREE (Fig. 5c).

Discussion

New findings from mafic and felsic minerals at site 296

DSDP Site 296 presents a unique opportunity to study the evolution of arc magma in the northernmost section of the Oligocene IBM (KPR segment 1 from Ishizuka et al. (2011b)). Prior studies on the KPR in this region were made on dredged and piston core samples of plutonic and volcanic rocks (Haraguchi et al. 2003, 2012; Ishizuka et al. 2011b). Studies of contemporaneous sediments are from

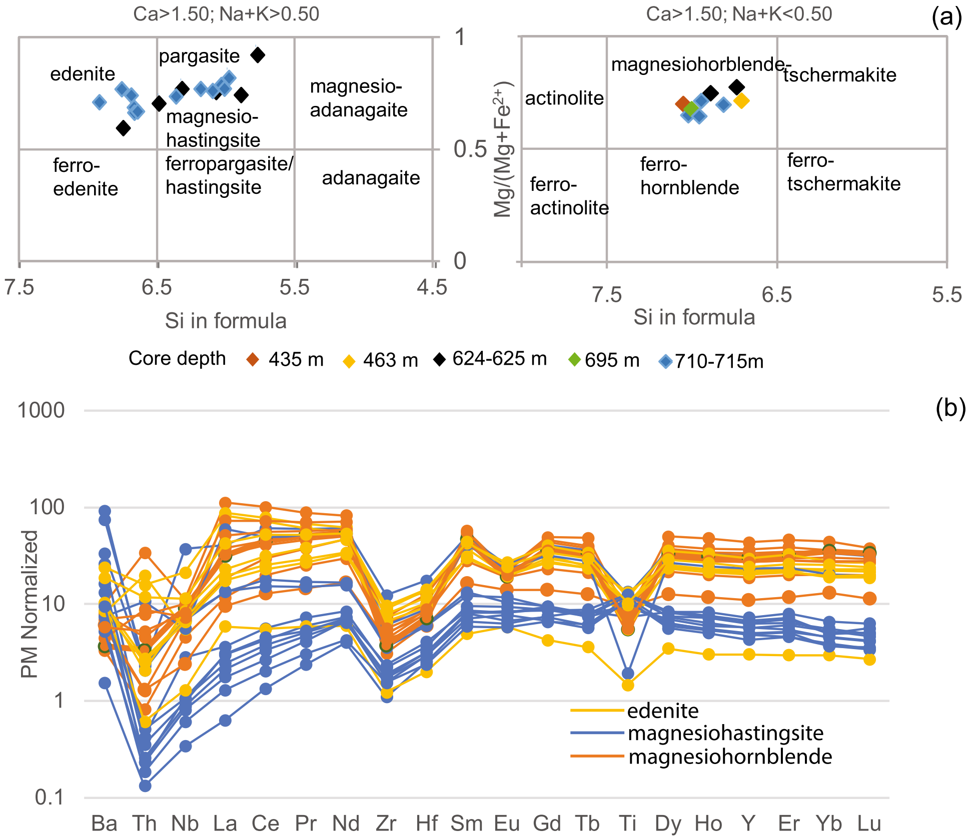

Fig. 4 **a** Site 296 amphibole compositions plotted using cationic values based on 23 Oxygens after Leake et al. (1997). **b** Primitive mantle normalized trace element abundances in amphiboles

a volcaniclastic sequence in the adjacent Amami-Sankaku basin drilled at IODP Site U1438 which range in age from Late Eocene to late Oligocene (Arculus et al. 2015b; Brandl et al. 2017; Barth et al. 2017; Hamada et al. 2020). In the IBM forearc, Oligocene ashes and tephra were drilled at ODP Site 782 (Straub 2003, 2008; Bryant et al. 2003). Because it is situated in a basin near the crest of the KPR, Site 296 records the magmatic evolution of the early–late Oligocene IBM arc, up until arc rifting and opening of the Shikoku basin.

Fresh glass shards provide the best magmatic record of melt compositions, (Lee et al. 1995; Samajpati and Hickey-Vargas, 2020), but preservation of a large quantity of fresh and undevitrified glass in older volcaniclastic sediments is uncommon (Arculus et al. 1995; Lee et al. 1995). Compared to glass, mafic minerals like pyroxene and amphiboles are more resistant to alteration and more abundant. Pyroxenes at Site 296 are the dominant mafic silicate grains and are present throughout the stratigraphic section. The composition of the Site 296 cpx was used to distinguish the tectonomagmatic affinities of the cpx (Fig. 6a–c) using the discrimination diagram of Leterrier et al. (1982). The result shows that these cpx are mostly from subalkaline magma, showing both calc-alkaline and tholeiitic affinities, and a few are MORB-like. Stratigraphically, calc-alkaline cpx are predominant in the bottom cores whereas tholeiitic ones are more common at the top. This is similar to the observation of Brandl et al. (2017) and Hamada et al. (2020) based on cpx within the Eocene to late Oligocene section at IODP Site 1438. The few MORB-like cpx at Site 296 occur at the top of the section.

Amphiboles in early IBM magmas represented by tephra fragments in IBM forearc cores were associated with felsic melt compositions by Straub (2008) but there is limited evidence of amphibole crystallization based on the trace element concentrations of Site 296 mafic through felsic glass shards and lithic fragments found in Unit 2 (Samajpati and Hickey-Vargas 2020). In contrast, pristine amphibole crystals are found as isolated grains in Site 296 sediments which indicates that amphiboles must have been phenocrysts in early IBM volcanic rocks.

The only felsic mineral in the Site 296 sediment is plagioclase (An$_{45–95}$). No quartz or muscovite was found. In terms of An content, presence of > An$_{90}$ plagioclase is commonly attributed to high H_2O content of arc magma as high-water content suppresses Si–O–Si–O polymerization and favors crystallization of anorthite over albite (Sisson and Grove 1993). In following sections, we utilize published experimental tools to understand the origins of the minerals, which together with glass shard compositions, refine and add to our knowledge of the evolution of the early IBM arc.

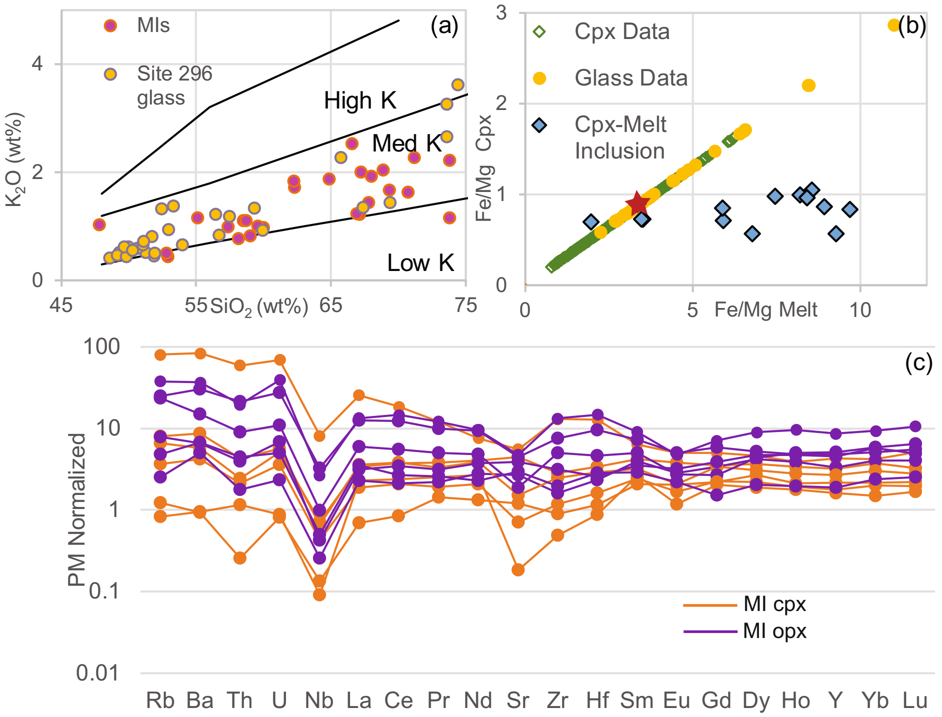

Fig. 5 **a** K$_2$O vs SiO$_2$ showing Site 296 melt inclusions in clinopyroxene compared with detrital glass shards from Site 296. Glass shard data are from Samajpati and Hickey-Vargas (2020) **b** Cationic Fe/Mg ratios for melt inclusions and host clinopyroxenes. Kd line for cpx/melt is 0.27 after Putirka (2008). Clinopyroxene Fe/Mg calculated from Site 296 glass shards and melt Fe/Mg calculated from Site 296 clinopyroxenes are plotted on the equilibrium line to show the range of values. The melt inclusion (red star) which plots on the equilibrium line is of a basaltic composition and has been used to calculate partition coefficients; two other inclusions also lie close to the line. **c** Primitive mantle normalized trace element compositions of melt inclusions from clinopyroxenes (orange) and orthopyroxenes (purple)

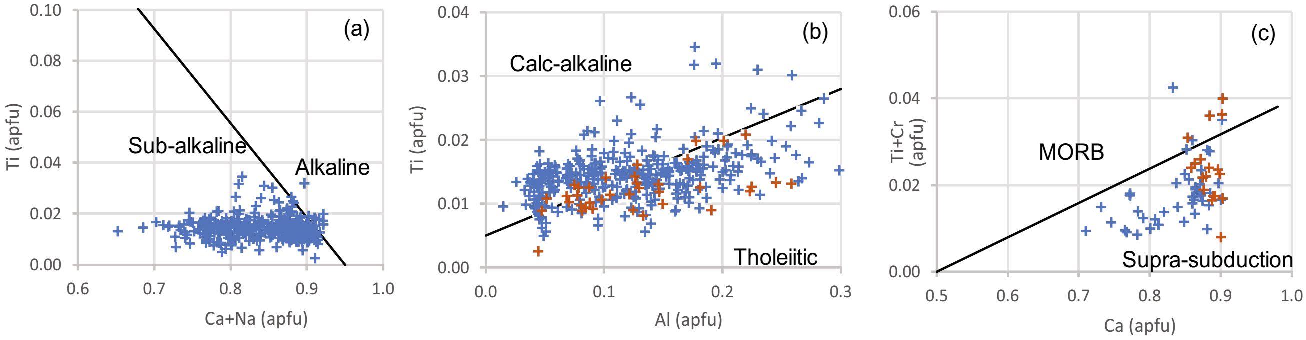

Fig. 6 **a–c** Tectonic discrimination diagrams based on clinopyroxene compositions from Leterrier et al. (1982). Elements are expressed in cationic value from the structural formula of clinopyroxenes. Orange symbols in **b** and **c** are the unusually high-Mg# clinopyroxenes discussed in the text. Fewer data points are shown in c because Cr was not analyzed

Inferences from clinopyroxenes

Mg-numbers of clinopyroxenes and coexisting melts

The distribution coefficient (Kd) of an element is defined as the ratio of its concentration in a mineral to its concentration in the melt, is a measure of the preference of that element in a given phase and can be used to model magmatic processes (e.g., O'Hara 1995; Shaw 2000). Figure 5b shows the Mg# of liquids inferred from the composition of Site 296 cpx compared with the Mg# of glass shards (Samajpati and Hickey-Vargas 2020) found in Unit 2, with reference to the Kd$_{(Fe–Mg)}$ between melt and cpx (Putirka 2008). Glasses representing the most primitive melts inferred from the cpx are not found in the core and were either not erupted or not preserved. Additionally, none of the cpx apparently crystallized from the most silicic melts represented by the glass shards. In this case, the melts may not have been saturated with cpx, or cpx crystallization may have been impeded by rapid cooling of the felsic melts. The most primitive cpx, with Mg# of 88–92, were calculated to coexist with melts having Mg# between 67 and 73, which is higher than that observed in the late Oligocene IBM melts represented by either glass, ash or lava, although Brandl et al. (2017) report similar high-Mg# in both cpx and its hosted MIs in the > 37 Ma (Eocene) section of IODP Site 1438. Cpx with Mg# between 87 and 61 are in equilibrium with melts of Mg# 65–30, which comprises a range of mafic to felsic lavas (45–69 wt% SiO_2) seen in the late Oligocene products. Some of the most primitive KPR basaltic lavas reported by Haraguchi et al. (2012) and Ishizuka et al. (2011b) had Mg# 65–63. Ash particles studied by Straub (2003) with a range from Mg# 47 to 30 have silica contents between 56 and 69 wt% similar to Site 296 glasses (Samajpati and Hickey-Vargas 2020), although more silicic melts inferred from glass and tephra have been reported in Sites 296 and 782A. The conclusion of this comparison is that the range of melt compositions inferred from cpx extends to more mafic melts than found among the glasses but does not reach that of the most felsic glasses.

The composition of all cpx grains from Site 296 define a broad trend in the variation of Al_2O_3 with the Mg# (Fig. 7). Overall, Al_2O_3 contents increase to a maximum of about 7 wt% near Mg# = 80 and then decrease at lower Mg#s. That the alumina content of the most magnesian cpx increases as Mg# decreases from 92 to 86 suggests that the magnesian cpx crystallized from magma without accompanying plagioclase, consistent with the suppression of plagioclase crystallization at high pressure and/or water contents (Kay and Kay 1985; DeBari et al. 1987; DeBari and Coleman 1989). Alternatively, because the Al content in cpxs also increases as a function of pressure (Nimis and Ulmer 1998), the low alumina contents of cpx may be related to lower pressures of crystallization. Using this reasoning, the cpx with highest Mg# and low alumina probably crystallized in a shallow or low-pressure environment. In contrast, the wide variation in Al contents at Mg# ~ 80 could be a result either of the generation of magma at different depths or variable alumina contents of the magma as the result of varying co-precipitation of plagioclase with other minerals, or both these processes occurring together. The broadly decreasing trend in the alumina content with further decreasing Mg# may indicate the onset of plagioclase crystallization together with cpx during differentiation to form silicic magmas.

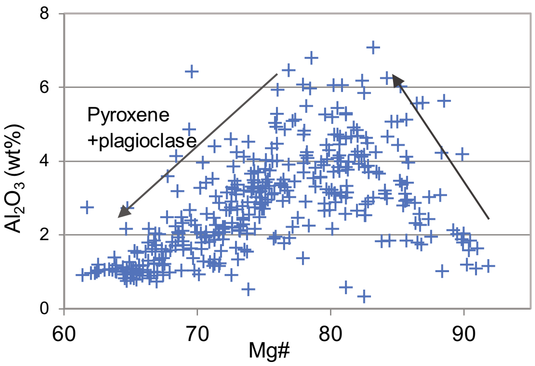

Fig. 7 Al_2O_3 vs Mg# for Site 296 clinopyroxenes. See text for explanation

Pressure estimates using clinopyroxene thermobarometry

Pressure estimates from clinopyroxene are calculated as a linear function of unit-cell and M site volume (Nimis 1995; Nimis and Ulmer 1998; Nimis 1999). For hydrous magmas like those of subduction zones, the barometer is also sensitive to the temperature of crystallization and a close estimation of temperature (± 50 °C) is needed to give accurate pressure readings. For Site 296 pyroxenes, in sediments, it is difficult to estimate a temperature using other geothermometers. To estimate pressure, a temperature was chosen based on a temperature determined on pyroxenes from lithic clasts from volcaniclastic sediments shed from the KPR and drilled at ODP Site 1201 (D'Antonio et al. 2006), giving a result of 1155 ± 56 °C for the most primitive magmas. ODP Site 1201 has IBM debris contemporaneous in age to Site 296 but is located in segment 3 of KPR (Ishizuka et al. 2011b) roughly 1100 km south of Site 296. Using the cpx geobarometer (Nimis 1999) at temperatures of 1155 °C some high-Mg# cpx (88–92) produced negative pressures, indicating these cpx compositions probably formed at lower temperatures. At 1100–1075 °C, most high-Mg# cpx yield a pressure of crystallization of 0–2 kbar, and those with both high-Mg# and high Al content (Fig. 7) give 4–6 kbar pressure of crystallization. Cpx with lower Mg numbers between 78 and 84 gave pressures ranging from 0 to 8 kbar at temperatures of 1100–1075 °C. Because of the sensitivity of the barometer to Al contents of magma, only low Al mafic magmas provide an accurate pressure estimate (Nimis 1999). The higher pressures given by the high Al cpx could reflect either crystallization in deeper magma reservoirs or their derivation from high alumina parent magmas.

Melt trace element concentrations and patterns estimated using clinopyroxene partition coefficients

Partitioning of trace elements between melt and crystal is affected by pressure, temperature, the composition of magma and the structure of the solid phase (Blundy and Wood 2003; Nandedkar et al. 2014, 2016; Shimizu et al. 2017; Humphreys et al. 2019). At subduction zones, water also plays a vital role in partitioning, as it may decrease the trace element activity in melts and cause preferential stability of one valence over the other (Blundy and Wood 2003). For this study, we calculated cpx/melt trace element Kds using the Site 296 cpx-hosted MIs, including basaltic, andesitic and dacitic inclusions and enclosing cpx, with results shown in Fig. 8. For comparison, and to test the efficacy of this approach, we show Kds from experimental studies having melt compositions similar to those inferred for the Site 296 cpx (Fig. 8 and caption). Phenocryst-matrix measurements were used when experimental data were not available. Partition coefficients for basalt were calculated from the Site 296 mafic cpx-basaltic MI that falls on the $Kd_{Fe\text{-}Mg}$ equilibrium line in Fig. 5b (red star) ensuring that post entrapment element exchanges were minimal. As shown in Fig. 8, Kds calculated from MI have similar trace element trends to those resulting from experiments, for example, similar relative values for different elements and REE Kd's that increase exponentially with more SiO_2-rich melt inclusions (Fig. 8). Therefore, for cpx without MIs, we used the Kd's calculated from the cpx and enclosed basaltic melt inclusion shown in Figs. 5b and 8 (Online Resource 6), applied only to mafic cpx (Mg# > 75).

Figure 9 shows the calculated trace element patterns for melts coexisting with high-Mg# cpx (88–92) and cpx with Mg# between 75 and 87. Patterns calculated from the highest Mg# cpx have a flat REE distribution and low concentrations of incompatible trace elements compared to glass shards from the Site 296 drill core (Samajpati and Hickey-Vargas 2020). Calculated trace element patterns for melts coexisting with cpx with Mg# 75 to 85 vary widely, from flat REE patterns to LREE enriched patterns. Cpx with Mg# of 86–87 yield melt trace element patterns that are similar to those inferred from the highest Mg# cpx and are grouped with them in Fig. 3b. Some of these calculated melts have higher Nb contents than LREE in the PM normalized multi-element

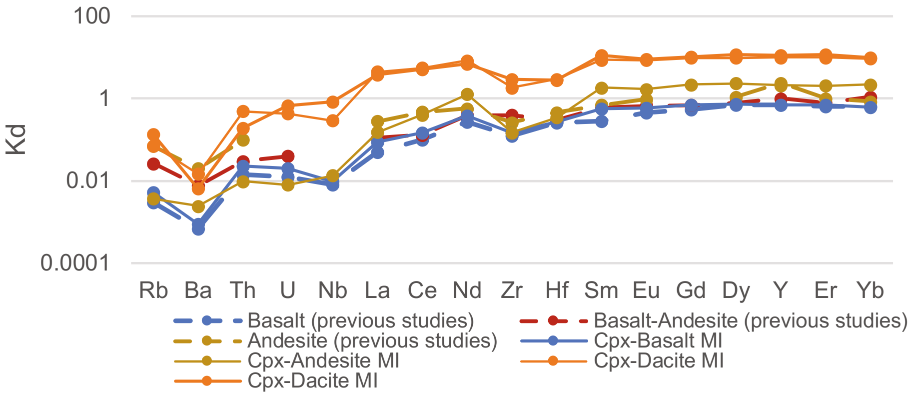

Fig. 8 Comparison of clinopyroxene/melt partition coefficients from basaltic, andesitic and dacitic melt inclusions and host cpx from Site 296, with published partition coefficients from experimental studies. For basaltic melts:-Rb-Klemme et al. (2002); Sm-Johnson (1994) Ce Y- Jenner et al. (1993); Ba, Zr, Hf- Hart and Dunn (1993); Th, U, La, Nd, Eu, Dy, Er, Yb, Lu- Hauri et al. (1994); Gd-Hack et al. (1994). For basaltic-andesite melts -Rb-Philpotts and Schnetzler (1970); Y, Zr, La, Ce, Nd, Sm, Dy, Er, Yb- Ronov and Yaroshevskiy (1976); Ba-Hart and Brooks (1974); Gd- Gallahan and Nielson (1992); Hf, Th, U- Dostal et al. (1983). For andesitic melts: La, Sm, Dy, Yb- Nicholls and Harris (1980); Zr- Watson and Ryerson (1986); Rb, Y-Ewart and Griffin (1994); Ba, Nd- Luhr and Carmichael (1980); Th, Ce, Hf—Bacon and Druitt (1988); Er-Schnetzler and Philpotts (1970)

Fig. 9 Primitive mantle normalized trace element abundances in melts calculated from Site 296 clinopyroxenes using cpx-basalt MI partition coefficients. Grey shaded area represents the trace element abundances of Site 296 glass shards (Samajpati and Hickey-Vargas, 2020). High-Mg andesite from Bonin Ridge Escarpment is shown in dark grey (Ishizuka et al. 2006)

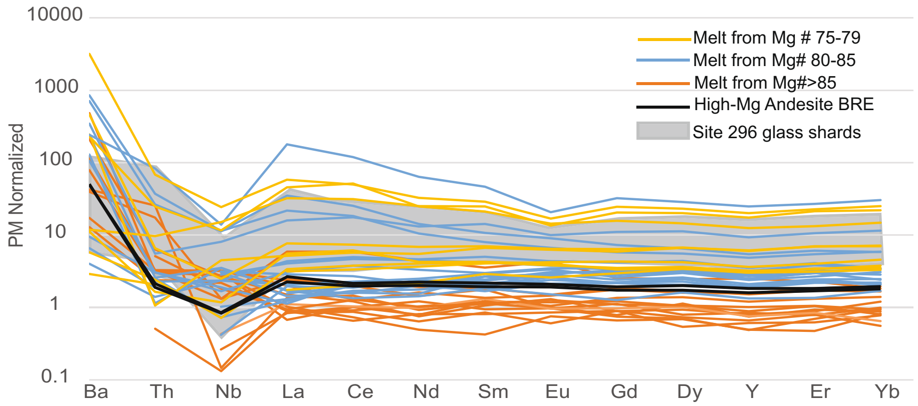

plot (Fig. 9) and therefore do not exhibit arc trace element characteristics (e.g., Perfit et al. 1980).

Inferences from amphiboles

Temperatures and magma compositions from amphibole compositions

Recent studies of amphibole compositions suggest that amphibole is not a reliable pressure indicator (Erdmann et al. 2014; Putirka 2016) except under restricted conditions like $T < 800$ °C and Fe# or $Fe/(Fe + Mg)$ amp < 0.65 (Anderson and Smith 1995). Amphiboles are more sensitive to temperature and liquid composition. Putirka (2016) emphasized that amphibole barometers based on partitioning of alumina between amphibole and melt (e.g., Ridolfi and Renzulli 2012) are only successful when multiple pressure estimates for different compositions are averaged, without which there could be an error of ± 4 kbar. In contrast, temperature estimates from amphibole compositions have a precision of ± 30 °C. We used the pressure (P-) independent thermometer from Putirka (2016), as given as Eq. 5, to estimate the temperature and Eq. 10 to determine the SiO_2 content of melts coexisting with Site 296 amphiboles. Results are temperatures of crystallization from 741 to 1016 °C for the amphiboles and silica contents for coexisting melts ranging from basaltic andesite to rhyolite (52–75 wt%). Magnesiohastingsites yield higher temperatures than magnesiohornblende. Magnesiohastingsites, crystallized at temperatures of 1016–872 °C, are more common in mafic to intermediate magmas (calculated SiO_2 52–66 wt%), whereas edenite and magnesiohornblendes are more common in silicic magmas (calculated SiO_2 69–75 wt%). The amphiboles crystallizing in basaltic andesite compositions are henceforth referred to as mafic amphiboles although these amphiboles do not have very high-Mg#s (62–67). Given the range of amphibole and melt SiO_2 compositions, the trace element variation in the amphiboles (Fig. 5b) may be related to the magma composition. The amphiboles which show low incompatible trace element concentrations mainly crystallized from mafic and intermediate magma. Among the mafic amphiboles, the variation in LREE is probably related to the geochemical characteristics of the primary magmas as LREEs are incompatible in mafic amphiboles. During differentiation from intermediate to silicic magma, plagioclase and titano-magnetite are usual major fractionating phases (Samajpati and Vargas 2020), and this probably explains the depletions of Eu and Ti in the normalized trace element patterns for silicic amphiboles. Apatite crystallization in silicic magma can also affect rare earth elements (REE); magma crystallizing apatite may have low concentrations of REE, especially MREE, and this might explain the differences among the silicic amphiboles (Prowatke and Klemme 2006).

Melt trace element concentrations estimated from composition matched amphibole-melt partition coefficients

Using SiO_2 contents inferred for melts coexisting with Site 296 amphiboles, we calculated melt trace element abundances using compositionally matched partition coefficients, as given by Nandedkar et al. (2016) and Humphreys et al. (2019) (Fig. 10a, b). We used both these sources to get a better comparison of data and to model the maximum number of trace elements. Partition coefficient values from Nandedkar et al. (2016) are listed in supplementary file (Online Resource 6). None of the calculated basaltic andesite (mafic) melt compositions calculated using these Kds show LREE depletion, although this is observed in some basalt or basalt-andesite glass shards from Site 296 (Fig. 10a). In Fig. 10, there are also some highly LREE enriched melt compositions inferred from amphibole compositions that are not observed among Site 296 glasses.

We also tested the multiple regression method from Humphreys et al. (2019) to calculate melt trace compositions in equilibrium with the Site 296 amphiboles. This method is empirical, based on multiple regression analysis of the major element composition of individual amphiboles and coexisting melts to calculate their individual trace element partition coefficients. Representative sets of example partition coefficients calculated using these methods are given in Online Resource 6. When the two sets of calculated melt compositions are compared, Kd values from Nandedkar et al. (2016) produced trends of highly elevated LREE over other rare earth elements (Fig. 10a) whereas using Humphreys et al. (2019) methods produced slightly elevated LREEs and more depleted HREEs in some felsic melts (Fig. 10b), all in comparison with Site 296 glass compositions. Overall, trace element abundance patterns calculated using Kds from Humphreys et al. (2019) have a better fit to the range of Site 296 detrital glass shards. Calculated La/Sm_N values using Kds from Humphreys et al. (2019) for basalt-andesite are 1.1 to 7.2, indicating the magma crystallizing amphibole was enriched in LREEs. Calculated trace element patterns for basaltic-andesite and andesite magmas using both sets of Kds have a positive Sr peak (Fig. 10a and b), indicating plagioclase was not an important fractionating phase at these magma compositions. In contrast, plagioclase was a major fractionating phase in the silicic magmas as inferred from the depletion of Sr in the plots.

Magma compositions based on amphibole stability in Island Arc Magmas

Understanding amphibole stability in volcanic rocks and especially in island arcs is an issue of great importance for understanding the evolution of the continental crust

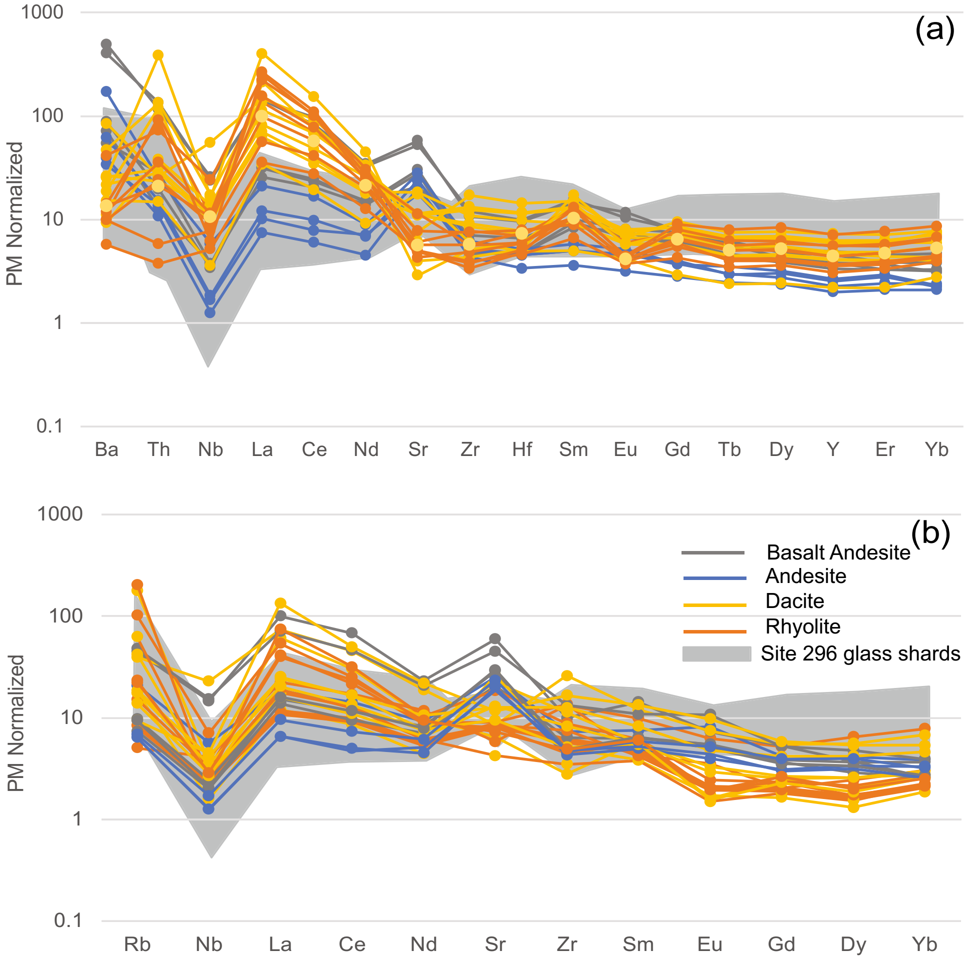

Fig. 10 **a** Primitive mantle normalized trace element abundances in melts calculated from amphiboles using amphibole/melt partition coefficients from Nandedkar et al. (2016). The shaded field represents the trace element abundances of Site 296 glass shards (Samajpati and Hickey-Vargas, 2020). **b** Calculated melt compositions using the method of Humphreys et al. (2019). The regression equation for Y and Ho from Humphreys et al (2019) produced anomalous peaks in the inferred melt trace element patterns which was not observed in the normalized trace element analyses for amphiboles, hence these elements are not plotted

(Davidson et al. 2007; Larocque and Canil 2010; Smith 2014). Stagnation of magma at intermediate crustal depths can stabilize amphiboles to a minimum of about 1.5–2 GPa (Allen and Boettcher 1983) under water-saturated conditions but magma degassing during ascent can destabilize amphibole. A slow ascent can cause the amphibole to break down into anhydrous minerals and fluid. In arc magmas, amphiboles are more common in intermediate and felsic rocks presumably because these are cooler and may have higher water contents. Therefore, the presence of mafic amphiboles in equilibrium with inferred melts with 52–56 wt% SiO_2 at Site 296 is relatively unique. Experiments conducted to address amphibole stability in arc magma revealed that Na_2O (at least 3 wt%) in addition to high water contents of the magma are crucial factors in stabilizing amphibole in hydrous high alumina basalts and basalt andesites (Sisson and Grove 1993). In lower Na_2O magmas, amphiboles start to appear only when andesite compositions are reached (Sisson and Grove 1993). Experiments of amphibole stability in primitive high-Mg andesites and basaltic andesites in arc magmas at variable water, pressure and fO_2 contents (Krawczynski et al. 2012) yielded high-Mg# amphiboles (Mg#s 76–82) coexisting with olivines at pressures over 500 MPa and temperatures of 975–1025 °C under high water contents (10–14 wt%). Such high-Mg# amphiboles are absent in Site 296, thereby suggesting that such primitive magmas are probably not the origin for these amphiboles.

We used the experimental major element Kds between amphibole and melt from Sisson and Grove (1993) to understand more about the major element composition of the melts. We used Kd_{Al-Si} since it is restricted to 0.94 in different melt compositions, compared to Kd_{Fe-Mg} which varies from 0.30 to 0.38 in mafic and intermediate melts to lower values in silicic melts (Sisson and Grove 1993). The calculated melts from which the mafic amphiboles crystallized have higher Al/Si ratios (0.36–0.43) than those observed in the more mafic glasses from Site 296 (0.28–0.36). This could mean that the mafic amphiboles crystallized from more alumina rich magmas than those represented by the Site 296 glass shards (11.4–15.5 wt%, Samajpati and Hickey-Vargas (2020)). We used the calculated melt major element composition from Site 296 amphiboles (Zhang et al. 2017; Humphreys et al. 2019) which yielded 18.0–18.7 wt% Al_2O_3 and MgO 2.1–5.3 wt% for basalt-andesites. The composition is similar to the low Mg high alumina hornblende diorites (equivalent to basaltic andesite) from experiments by Sisson and Grove (1993), where amphiboles started crystallizing at 998 °C with olivine and before plagioclase crystallization. Therefore, based on the major element calculated compositions and previous experimental studies, the mafic amphiboles might have crystallized from high alumina basaltic andesite magma with low to moderate MgO and at least 3 wt% Na_2O concentrations.

Synthesis: magma compositions recorded at site 296 and other locations in KPR segment 1

Figures 11, 12 and 13 summarize geochemical features of magma compositions inferred from minerals in the Site 296 section and analyses of glass shards. In this section, we interpret their origin and timing together with findings from other locations in KPR Segment 1. We group magma compositions into high-Mg#, flat to LREE-depleted and high Al_2O_3, LREE-enriched types.

High-Mg magmas

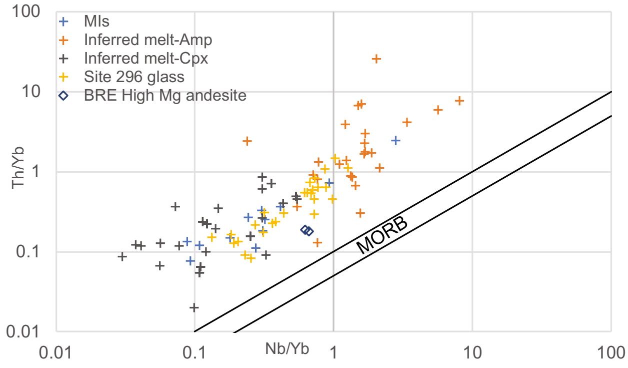

Fig. 12 Logarithmic plot of Th/Yb vs Nb/Yb for melt composition, both analyzed (Samajpati and Hickey-Vargas 2020; this study) and inferred from mafic minerals; also includes high-Mg andesite data from the Bonin Ridge Escarpment (BRE) (Ishizuka et al. 2006). Th concentrations for amphiboles are calculated using Th partition coefficients from Nandekar et al. (2016) as the Humphreys et al (2019) study did not include an equation for Th

IODP Site U1438 (Fig. 1a), situated about 240 km SW from Site 296 in the Amami Sankaku basin is also a part of segment 1 of the KPR. Both sites have contemporaneous records, but Site U1438 has a complete stratigraphic record starting from the igneous basement through Eocene and Oligocene volcaniclastic sediment (Arculus et al. 2015b; Brandl et al. 2017). At Site 296, these older records are absent except for one volcanic rock fragment dated at 47.5 Ma (Eocene) in a deep sandstone section (core 63) (Ozima et al. 1977). At IODP Site U1438, Brandl et al. (2017) found that high-Mg# melt inclusions within high-Mg cpx (Mg# 89 to 92) were found only in the older > 37 Ma sediments and were chemically similar to plagioclase poor (1–4%) high-Mg andesites of the Bonin Ridge Escarpment (BRE) (Fig. 1a). The origin of the BRE high-Mg rocks was inferred to occur during the change from decompression melting accompanying subduction initiation to early arc magma formation at about 44 Ma (Ishizuka et al. 2006). When compared to Site 296 high-Mg# cpx (Fig. 9), the inferred melts that formed the Site 296 high-Mg# cpx and BRE high-Mg-andesites have similar flat REE patterns and high Sr contents compared to

Fig. 11 Primitive mantle normalized REE plot for analyzed and calculated melts for all materials at Site 296. Compositional ranges inferred from clinopyroxenes, amphiboles and analyzed melt inclusions are shown as shaded fields, lines are individual glass shard and clast composition (Samajpati and Hickey-Vargas 2020). Normalizing values are from Sun and McDonough (1989)

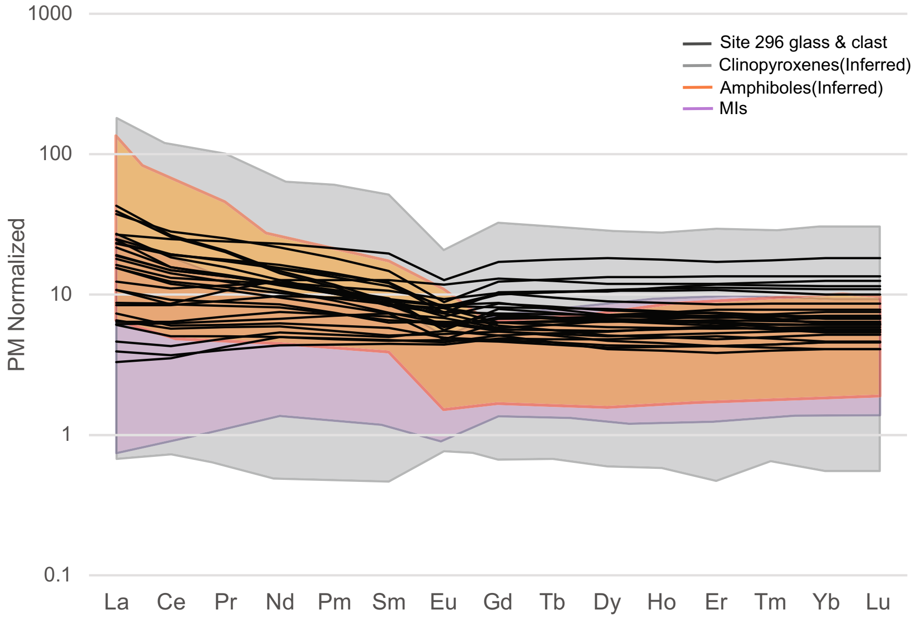

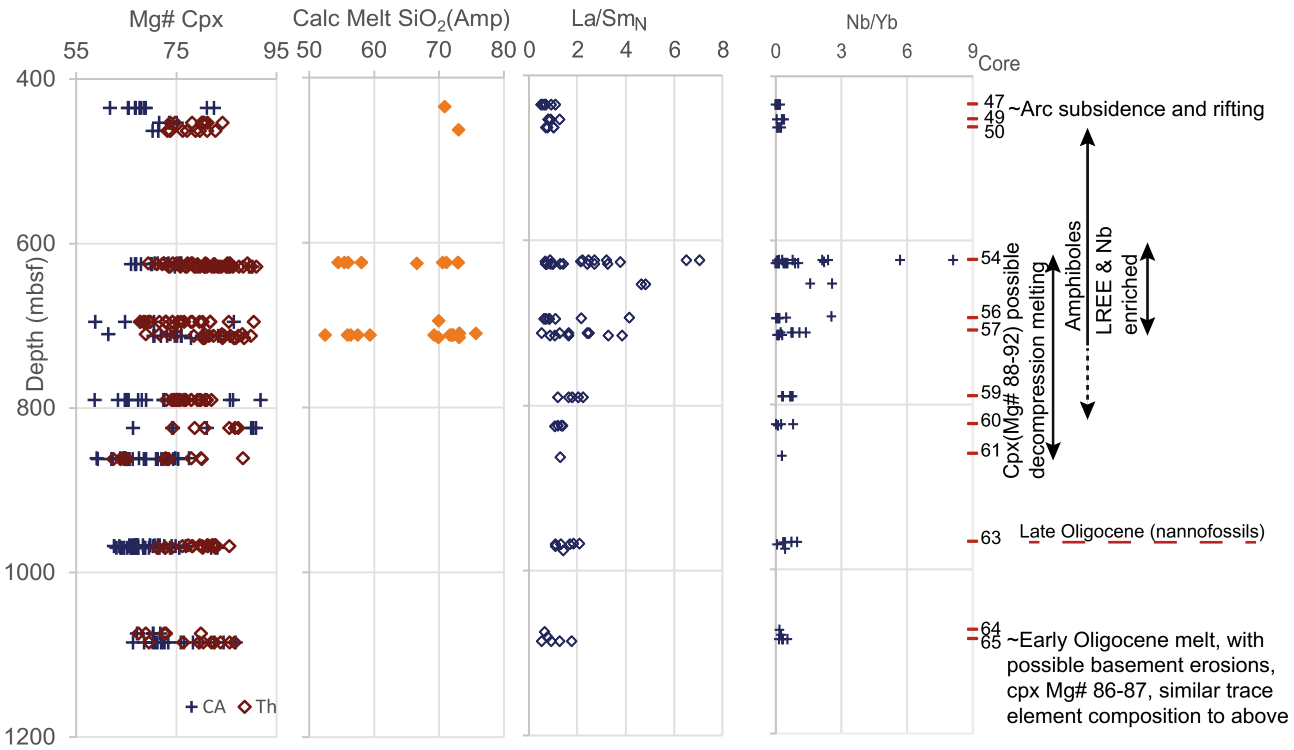

Fig. 13 From left to right, plot showing the depth vs Mg# of clinopyroxenes with their magmatic affinity; SiO_2 content of melt in equilibrium with amphibole; La/Sm_N of mafic to intermediate glass shards and calculated melts from clinopyroxene and amphibole; and Nb/Yb of mafic to intermediate glass shards and calculated melts

REE (Fig. 9), suggesting these magmas were not yet saturated with plagioclase. The high-Mg#-cpx of Site 296 also have low alumina content (Fig. 7) and inferred crystallization pressure of 0–2 kbar, suggesting that they formed in a shallow setting. In contrast to Site 1438, at Site 296, high-Mg# cpx appear predominantly in the upper-middle section of Unit 2 between cores 54 to upper 61 at approximate depths of 625–863 m. At this level, lapilli and ash tuffs are the dominant lithologies suggesting that the cpx were deposited directly during volcanic eruptions. Benthic foraminifera species in cores 55 and 56 indicate a near sea level location of late Oligocene age (Ingle et al. 1975). Therefore, magmas crystallizing these cpx are unlikely to have formed at the same time as the geochemically similar high-Mg andesites of the BRE or the melt inclusions in high-Mg cpx from > 37 Ma sediments at Site U1438. There are, however, cpx with Mg# of 87 in the deepest Site 296 core (core 65) with inferred melt trace element patterns similar to the other Site 296 high-Mg# cpx and BRE rocks. These could have been deposited directly during early Oligocene or older volcanic activity, or alternatively, included as eroded sediment or xenolithic fragments from older KPR volcanic products. In either case, it is plausible that this magma type, having low concentrations of incompatible trace elements and flat REE patterns reflects a particular tectonic regime. According to (Brandl et al. 2017), the BRE high-Mg andesites were pre-arc rocks formed during the transition from seafloor spreading associated with subduction initiation and true subduction and generation arc magma. By analogy, magmas forming the high-Mg# cpx at Site 296 might be related to the onset of arc extension, rifting and decompression melting during the late Oligocene. This interpretation is consistent with their low Al and shallow inferred crystallization depths and might also explain why high-Mg# cpx are absent in younger < 37 Ma sediments at Site U1438 on the non-rifted, rear arc side of the early IBM arc (Brandl et al. 2017).

LREE enriched magmas

Strongly LREE-enriched and high Al2O3 melt compositions are found in Site 296 in some glass shards (Samajpati and Hickey-Vargas (2020) and among mafic and intermediate magma compositions inferred from amphiboles. These also have REE patterns similar to strongly LREE enriched hornblende-bearing andesite clasts ($La/Sm_N > 4$) from Site 296 (Samajpati and Hickey-Vargas 2020). LREE enriched compositions were also observed for melts inferred from two cpx grains (Mg#s around 80 and 4–6 wt% Al_2O_3, La/Sm_N 3–4) and an andesite melt inclusion within a cpx with 17.9 wt% Al_2O_3 and $La/Sm_N = 4$. These compositions are comparable to highly LREE enriched volcanic rocks recovered from Nichinan seamount, located 160 km NW of Site 296 on the KPR (Haraguchi et al. 2012). All of the above materials, which point to LREE-enriched high-Al magmas as their source, are present in the topmost section of Unit 2, cores 54–57.

Our interpretation is that these LREE-enriched high-Al magmas were formed under high pressure and/or water contents towards the later part of the late Oligocene. Evidence for high water contents and/or a deeper magma reservoir is both the stabilization of amphibole and increasing dominance of calcic plagioclase at the middle to top of the stratigraphic section (Fig. 2). At high pressures and/or water content amphiboles are stabilized, and plagioclase crystallization is suppressed as the volume of stability of clinopyroxene expands (Baker and Eggler 1983). When plagioclase does crystallize, it is more Ca rich and Si poor with compositions of $An_{90–95}$ (Arculus and Wills 1980), as seen at Site 296.

Evidence for mantle depletion and enrichment

There is an upward increase in Nb/Yb ratios among inferred melt compositions in the Site 296 core (Fig. 13, cores 54–57). In Fig. 10b, the composition-matched trace element abundances of mafic and intermediate melts inferred from amphiboles at Site 296 using the method of Humphreys et al. (2019) vary from slightly to highly enriched in terms of La/Sm_N (1–7) and from Nb/Yb = 0.9 to 8.1. Th concentrations for the melts calculated using the composition-matched partition coefficients from Nandedkar et al. (2016), yield Th/Yb values that also vary widely 1–7. The most LREE-enriched mafic melt (SiO_2 = 55 wt%; La/Sm_N = 7.0) has the highest Nb and Th concentrations and highest Nb/Yb and Th/Yb ratios (8.1 and 7.6, respectively), which indicate high mantle fertility in the first case and incorporation of a subduction component in the second case (Brandl et al. 2017; Pearce et al. 2005).

Melt compositions calculated from the cpx do not show such high Nb/Yb but more moderate to extremely low values (Fig. 12). The extremely low values (close to and lower than 0.1 in Fig. 12) inferred from cpx could result from measurement errors due to the low, near detection limit, concentrations (Table 1), however, there are melt inclusions and glasses from Site 296 with higher Nb concentrations whose Nb/Yb values are close to 0.1 (Fig. 12). Since Nb/Yb is an indicator of mantle fertility (Pearce et al. 2005), the wide variation of Nb/Yb ratios in Fig. 12 suggests changes in mantle source fertility took place between the formation of enriched magmas, as inferred from some amphiboles in cores 54–57 and depleted magmas inferred from cpx (Fig. 13). As seen in Fig. 13, diverse magmas in terms of La/Sm_N (~0–2) and Nb/Yb (0–1) are present throughout the Oligocene with the appearance of highly enriched (La/Sm_N = 7; Nb/Yb = 8) and amphibole bearing magmas shortly before the cessation of volcanism marking arc rifting. In short, we can suggest towards the late Oligocene, deep-seated magma storage or high-water contents of the magma may have led to the evolution of high Al magmas with variable Mg contents from a somewhat LREE and Nb enriched source with the crystallization of high-Al cpx, amphiboles, and highly calcic plagioclases.

Temporal changes and oligocene rifting of the early IBM arc

Rifting of the KPR and opening of the Shikoku basin by sea-floor spreading was interpreted to have begun by the late Oligocene at about 30 Ma (Okino et al. 1994; Ishizuka et al. 2011b). Our results suggest that the formation and eruption of high-Mg, incompatible element-poor shallow-source decompression melts may have started at this time within the early IBM, and was gradual, with intermittent periods of decompression melting related to arc extension and typical arc magmatism. Figure 13 shows the temporal or stratigraphic changes at Site 296 in terms of mineral compositions present and geochemical characteristics observed. Considering the lowermost cores of Unit 1 (core 47) and cores of Unit 2 at Site 296 together, there is a gradual change upward in La/Sm_N and Nb/Yb in magma from depleted to slightly enriched (cores 59–65) to highly enriched (cores 54–57) and then again to depleted at the top (cores 47–50) (Fig. 13). The abrupt change from highly enriched, high Nb/Yb, to depleted characteristics at the base of Site 296 Unit 1 (around core 47) might mark the final shift to rifting and related decompression melting. Brandl et al. (2017) also interpreted, based on melt inclusions within cpx from IODP Site U1438 Unit III, that there was an increase in the Nb/Yb in melt compositions prior to rifting. The subsequent decrease was not apparent in the Site U1438 section, although a small subset of MIs at 30 Ma was identified as low-P melts by Hamada et al. (2020).

The highly LREE-enriched and high Nb/Yb late-stage mafic magmas at Site 296 are inferred from amphiboles in and above core 57 in Unit 2. The enriched characteristics of these magmas and presence of amphiboles reflect high water pressure conditions that may have developed as the arc crust thickened and matured, and magma became enriched in water and fluid mobile elements from the subducted slab. As noted above, depleted magma (La/Sm_N 0.5–1, Nb/Yb close to 0.1) compositions occur in the same stratigraphic intervals as the enriched amphibole bearing magmas discussed above. Melts inferred from the high-Mg# cpx have characteristics implying shallow crystallization pressures (0–3 kbar at 1100 °C), both calc-alkaline and tholeiitic types (Fig. 6c). The presence of such enriched and depleted magmas together implies that diverse magmas may have formed from different depths and by different processes over the period represented by the Site 296 cored section. Therefore, it is highly likely that there were multiple stages of arc rifting, with accompanying decompression melting, and eruption of high-Mg, incompatible element poor melts from a depleted mantle source, alternating with eruption of incompatible element-enriched, hydrous, amphibole-bearing arc magmas from deep seated in the arc. Towards the top of Unit 2 (core 50), and base of Unit 1 (core 47), the change from enriched sources to more depleted sources having lower La/Sm_N and Nb/Yb in Fig. 13 together with lower Th/Yb (4 to~0) may reflect the decreasing subduction component to form arc magmas and increasing BABB (back arc basin basalt) component as extension and rifting became dominant.

Studies of sediments from IODP Site 1438 delineate the older Eocene to late Oligocene variation in early IBM magmas. Hamada et al. (2020 identified three major magma types between 30 and 40 Ma, enriched medium K tholeiitic magmas (30–38 Ma), enriched medium K calc-alkaline magmas (30–39 Ma) and depleted low K calc-alkaline magma (35–40 Ma). Brandl et al. (2017) interpreted, based on melt inclusions within cpx from IODP Site U1438 Unit III, that the arc changed from more calc-alkaline dominated primary melts within the > 37 Ma section to tholeiitic island arc differentiates within the < 37 Ma sections. At Site 296, melt compositions, whether inferred from minerals or from glass shards or MIs (Samajpati and Vargas 2020; this study), are of medium K (from glass shards and MIs) and both arc tholeiite and calc-alkaline series character. Since Site 296 section is largely late Oligocene, these findings are consistent with those from IODP Site U1438 (Brandl et al. 2017; Hamada et al. 2020).

Conclusions

Late Oligocene tuffs, lapilli tuffs and volcanic sandstones drilled at DSDP Site 296 on the Kyushu Palau Ridge contain abundant fresh pyroxene and amphibole grains, but fresh scarce glass shards and no unaltered volcanic clasts. This study utilizes studies of mineral-melt equilibrium to calculate melt compositions and conditions of magma crystallization, an approach that is useful where whole rocks are not preserved. At Site 296, the range of magma major and trace element compositions inferred from minerals exceeds that represented by the glass shards in the sediment and probably gives a more complete understanding of represented magma compositions and the sequence of magmatic evolution.

Using new data for melt inclusions in cpx, we estimate a new set of trace element partition coefficients for mafic cpx/melt and these are consistent with the trends of experimental studies. For amphibole, mineral/melt partition coefficients from Nandedkar et al. (2016) (experimental) and Humphreys et al. (2019) (empirical) were used. Calculated trace element abundances define three main magma types:

(1) slightly depleted to enriched (La/Sm_N 0.5–4) tholeiitic to calc-alkaline arc magmas similar to magmas represented by Site 296 glass shards; (2) late stage high-Mg magmas with MORB or BABB-like trace element signatures, and (3) also late stage highly LREE enriched (La/$Sm_N > 6$) and water-rich arc melts from a fertile mantle source.

Using mineral geothermobarometry, we infer that the crystallization conditions for cpx in magmas at Site 296 ranged from low pressure (0–3 kbar) for the low alumina, intermediate to highest Mg# cpx, in contrast to higher pressure (up to 8 kbar), water-rich and plagioclase-poor magmatic evolution for moderate alumina and intermediate and low Mg# (< 80) cpx.

Based on inferred magma chemistry and crystallization conditions, and stratigraphic considerations some unique findings for the early magmatic history of the IBM arc not well recorded in other sites are:

(1) During the late Oligocene, primary magmas with diverse incompatible element patterns formed and differentiated at different depths (0–30 km) Based on clinopyroxene compositions both calc-alkaline magmas and tholeiitic magmas were present, and these results are comparable and similar to Brandl et al. (2017) and Hamada et al. (2020) for the contemporaneous parts of the drilled section at IODP Site U1438.
(2) Shortly before arc rifting and opening of the Shikoku basin, highly incompatible element-enriched magmas formed from a fertile mantle source and crystallized as mafic amphibole-bearing arc lavas. These may have been derived from local point source like that producing the enriched magmas from nearby Nichinan Seamount (Haraguchi et al. 2012), or they may reflect a temporal change related to subduction conditions.
(3) Arc extension and production of BABB-like decompression melts occurred in multiple events before complete arc rifting and opening of the Shikoku basin. Magma formed during these events produced high-Mg# cpx from a depleted, MORB-like mantle sources.
(4) The time scale for these events is uncertain because both mafic amphiboles (late stage enriched arc magmas) and high-Mg# cpx (MORB-like magmas) are present in some of the same sampled intervals. This implies that both arc (IAB) and back-arc (BABB) types of magma coexist in arcs undergoing rifting and back-arc basin formation.

Supplementary Information The online version contains supplementary material available at https://doi.org/10.1007/s00410-022-01909-6.

Acknowledgements This research was supported by NSF grant OCE 15377861 to Rosemary Hickey-Vargas. We gratefully acknowledge the contribution of Gabriela Fernandez in preparing the smear slides for the core samples. We also thank Thomas Beasley of the Florida Center for Analytical Electron Microscopy (FCAEM) at FIU for assistance with EPMA analyses and Dr. Sarah Jantzi of the Trace Evidence Analysis Facility (TEAF) at FIU for assistance with LA-ICP-MS analyses.

References

Allen JC, Boettcher AL (1983) The stability of amphibole in andesite and basalt at high pressures. Am Miner 68(3–4):307–314

Anderson JL, Smith DR (1995) The effects of temperature and f (sub O2) on the Al-in-hornblende barometer. Am Mineralogist 80(5–6):549–559

Arculus RJ, Wills KJA (1980) The petrology of plutonic blocks and inclusions from the Lesser Antilles island arc. J Petrol 21(4):743–799

Arculus RJ, Bloomfield AL, Fryer P et al (1992) Major-element geochemistry of ashes from Sites 782, 784 and 786 in the Bonin forearc. Proc Ocean Drilling Program Scientific Results 125:277–292

Arculus RJ, Ishizuka O, Bogus KA et al (2015a) A record of spontaneous subduction initiation in the Izu-Bonin-Mariana Arc. Nat Geosci 8(9):728–733

Arculus R, Ishizuka O, Bogus K et al (2015b) International Ocean Discovery Program Expedition 351 preliminary report; Izu-Bonin-Mariana Arc origins; continental crust formation at an intraoceanic arc; foundation, inception, and early evolution; 30 May–30 July 2014: Preliminary Report (International Ocean Discovery Program), vol. 351

Arculus RJ, Gill JB, Cambray H, Chen W, Stern RJ, Taylor B, Natland J (1995) Geochemical evolution of arc systems in the western Pacific; the ash and turbidite record recovered by drilling. Geophys Monograph 88:45–65

Bacon CR, Druitt TH (1988) Compositional evolution of the zoned calcalkaline magma chamber of Mount Mazama Crater Lake, Oregon. Contrib Mineral Petrology 98(2):224–256

Baker DR, Eggler DH (1983) Fractionation paths of Atka (Aleutians) high-alumina basalts; constraints from phase relations. J Volcanol Geothermal Res 18(1–4):387–404

Barth AP, Tani K, Meffre S et al (2017) Generation of silicic melts in the early Izu-Bonin Arc recorded by detrital zircons in proximal arc volcaniclastic rocks from the Philippine Sea. Geochem Geophys Geosyst G3 18(10):3576–3591

Blundy J, Wood B (2003) Partitioning of trace elements between crystals and melts. Earth Planet Sci Lett 210(3–4):383–397

Brandl PA, Hamada M, Arculus RJ et al (2017) The arc arises; the links between volcanic output, arc evolution and melt composition. Earth Planet Sci Lett 461:73–84

Bryant CJ, Arculus RJ, Eggins SM (2003) The geochemical evolution of the Izu-Bonin Arc system; a perspective from tephras recovered by deep-sea drilling. Geochem Geophys Geosyst. https://doi.org/10.1029/2002GC000427

D'Antonio M, Savov I, Spadea P, Hickey-Vargas R, Lockwood J (2006) Petrogenesis of Eocene oceanic basalts from the West Philippine Basin and Oligocene arc volcanics from the Palau-Kyushu Ridge drilled at 20 degrees N, 135 degrees E (Western Pacific Ocean). Ofioliti 31(2):173–187

Davidson J, Turner S, Handley H, Macpherson C, Dosseto A (2007) Amphibole "sponge" in arc crust? Geology (boulder) 35(9):787–790

Debari SM, Coleman RG (1989) Examination of the deep levels of an island arc; evidence from the Tonsina ultramafic-mafic assemblage Tonsina, Alaska. J Geophys Res 94(B4):4373–4391

Debari S, Kay SM, Kay RW (1987) Ultramafic xenoliths from Adagdak Volcano, Adak, Aleutian Islands, Alaska; deformed igneous cumulates from the Moho of an island arc. J Geol 95(3):329–341

Dostal J, Dupuy C, Carron JP, Guen Le, de Kerneizon M, Maury RC (1983) Partition coefficients of trace elements; application to volcanic rocks of St. Vincent, West Indies. Geochim Cosmochim Acta 47(3):525–533

Elliott T, Plank T, Zindler A, White W, Bourdon B (1997) Element transport from slab to volcanic front at the Mariana Arc. J Geophys Res 102(B7):14991–15019

Erdmann S, Martel C, Pichavant M, Kushnir A (2014) Amphibole as an archivist of magmatic crystallization conditions; problems, potential, and implications for inferring magma storage prior to the paroxysmal 2010 eruption of Mount Merapi, Indonesia. Contrib Mineral Petrol https://doi.org/10.1007/s00410-014-1016-4

Ewart A, Griffin WL (1994) Application of proton-microprobe data to trace-element partitioning in volcanic rocks. Chem Geol 117(1–4):251–284

Gallahan WE, Nielsen RL (1992) The partitioning of Sc, Y, and the rare earth elements between high-Ca pyroxene and natural mafic to intermediate lavas at 1 atmosphere. Geochim Cosmochim Acta 56(6):2387–2404

Griffin W, Powell W, Pearson NJ, O'Reilly S (2008) GLITTER: data reduction software for laser ablation ICP-MS. In: Paul S (eds), Laser ablation–ICP–MS in the earth sciences current practices and outstanding issues 40, pp 308–311

Hack PJ, Nielsen RL, Johnston AD (1994) Experimentally determined rare-earth element and Y partitioning behavior between clinopyroxene and basaltic liquids at pressures up to 20 kbar. Chem Geol 117(1–4):89–105

Hamada M, Iwamori H, Brandl PA et al (2020) Temporal evolution of proto-Izu-Bonin-Mariana Arc volcanism over 10 myr; constraints from statistical analysis of melt inclusion compositions. J Petrology 61(1):egaa022

Haraguchi S, Ishii T, Kimura J, Kato Y (2012) The early Miocene (approximately 25 Ma) volcanism in the northern Kyushu-Palau Ridge, enriched mantle source injection during rifting prior to the Shikoku back-arc basin opening. Contrib Mineral Petrol 163(3):483–504

Haraguchi S, Ishii T, Kimura J, Ohara Y (2003) Formation of tonalite from basaltic magma at the Komahashi-Daini Seamount, northern Kyushu-Palau Ridge in the Philippine Sea, and growth of Izu-Ogasawara (Bonin)-Mariana arc crust. Contrib Mineral Petrol 145(2):151–168

Hart SR, Brooks C (1974) Clinopyroxene-matrix partitioning of K, Rb, Cs, Sr and Ba. Geochim Cosmochim Acta 38(12):1799–1806

Hart SR, Dunn T (1993) Experimental cpx/melt partitioning of 24 trace elements. Contrib Mineral Petrol 113(1):1–8

Hauri EH, Wagner TP, Grove TL (1994) Experimental and natural partitioning of Th, U, Pb and other trace elements between garnet, clinopyroxene and basaltic melts. Chem Geol 117(1–4):149–166

Hochstaedter A, Gill J, Peters R, Broughton P, Holden P, Taylor B (2001) Across-arc geochemical trends in the Izu-Bonin arc; contributions from the subducting slab. Geochem Geophys Geosyst G3 2(7):2000GC000105

Humphreys MCS, Cooper GF, Zhang J et al (2019) Unravelling the complexity of magma plumbing at Mount St. Helens: a new trace element partitioning scheme for amphibole. Contrib Mineral Petrol. https://doi.org/10.1007/s00410-018-1543-5

Ingle JC Jr, Karig DE, Bouma AH et al (1975) Site 296: Initial reports of the deep sea drilling project, vol. 31, pp 191–274

Ishizuka O, Kimura J, Li YB et al (2006) Early stages in the evolution of Izu-Bonin Arc volcanism; new age, chemical, and isotopic constraints. Earth Planet Sci Lett 250(1–2):385–401

Ishizuka O, Tani K, Reagan MK et al (2011a) The timescales of subduction initiation and subsequent evolution of an oceanic island arc. Earth Planet Sci Lett 306(3–4):229–240

Ishizuka O, Taylor RN, Yuasa M, Ohara Y (2011b) Making and breaking an island arc; a new perspective from the Oligocene Kyushu-Palau Arc, Philippine Sea. Geochem Geophys Geosyst G3 12(5):Q05005

Ishizuka O, Taylor RN, Umino S, Kanayama K (2020) Geochemical evolution of arc and slab following subduction initiation; a record from the Bonin Islands, Japan. J Petrol 61(5):egaa50

Jenner GA, Foley SF, Jackson SE, Green TH, Fryer BJ, Longerich HP (1993) Determination of partition coefficients for trace elements in high pressure-temperature experimental run products by laser ablation microprobe-inductively coupled plasma-mass spectrometry (LAM-ICP-MS). Geochim Cosmochim Acta 57(23–24):5099–5103

Johnson KTM (1994) Experimental cpx/ and garnet/melt partitioning of REE and other trace elements at high pressures; petrogenetic implications. Mineral Magazine 58A(A-K):454–455

Karig DE (1975) Basin genesis in the Philippine Sea: initial reports of the deep sea drilling project, vol. 31, pp 857–879

Kay SM, Kay RW (1985) Aleutian tholeiitic and calc-alkaline magma series; 1, The mafic phenocrysts. Contrib Miner Petrol 90(2–3):276–290

Klemme S, Blundy JD, Wood BJ (2002) Experimental constraints on major and trace element partitioning during partial melting of eclogite. Geochim Cosmochim Acta 66(17):3109–3123

Kobayashi K, Kasuga S, Okino K (1995) Shikoku Basin and its margins. Plenum Press, New York

Krawczynski MJ, Grove TL, Behrens H (2012) Amphibole stability in primitive arc magmas; effects of temperature, H (sub 2) O content, and oxygen fugacity. Contrib Mineral Petrol 164(2):317–339

Larocque J, Canil D (2010) The role of amphibole in the evolution of arc magmas and crust; the case from the Jurassic Bonanza Arc section, Vancouver Island, Canada. Contrib Mineral Petrol 159(4):475–492

Leake BE, Woolley AR, Arps CES et al (1997) Nomenclature of amphiboles; report of the subcommittee on amphiboles of the International Mineralogical Association, Commission on New Minerals and Mineral Names. Can Mineral 35:219–246

Lee J, Stern RJ, Bloomer SH (1995) Forty million years of magmatic evolution in the Mariana arc; the tephra glass record. J Geophys Res 100(9):17671–17687

Leng W, Gurnis M (2015) Subduction initiation at relic arcs. Geophys Res Lett 42(17):7014–7021

Leterrier J, Maury RC, Thonon P, Girard D, Marchal M (1982) Clinopyroxene composition as a method of identification of the magmatic affinities of paleo-volcanic series. Earth Planet Sci Lett 59(1):139–154

Luhr JF, Carmichael ISE (1980) The Colima volcanic complex, Mexico; I, Post-caldera andesites from Volcan Colima. Contrib Miner Petrol 71(4):343–372

Maunder, B., Prytulak, J., Goes, S., and Reagan, M., 2020, Rapid subduction initiation and magmatism in the Western Pacific driven by internal vertical forces. Nature Communications, v. 11, no. 1874.

Nandedkar RH, Ulmer P, Muntener O (2014) Fractional crystallization of primitive, hydrous arc magmas; an experimental study at 0.7 GPa. Contrib Mineral Petrol. https://doi.org/10.1038/s41467-020-15737-4

Nandedkar RH, Hurlimann N, Ulmer P, Muntener O (2016) Amphibole-melt trace element partitioning of fractionating calc-alkaline magmas in the lower crust; an experimental study. Contrib Mineral Petrol 171(8–9):71

Nicholls IA, Harris KL (1980) Experimental rare earth element partition coefficients for garnet, clinopyroxene and amphibole coexisting with andesitic and basaltic liquids. Geochim Cosmochim Acta 44(2):287–308

Nimis P (1995) A clinopyroxene geobarometer for basaltic systems based on crystal-structure modeling. Contrib Miner Petrol 121(2):115–125

Nimis P (1999) Clinopyroxene geobarometry of magmatic rocks Part 2 Structural geobarometers for basic to acid, tholeiitic and mildly alkaline magmatic systems. Contrib Mineral Petrol 135(1):62–74

Nimis P, Ulmer P (1998) Clinopyroxene geobarometry of magmatic rocks; Part 1, An expanded structural geobarometer for anhydrous and hydrous, basic and ultrabasic systems. Contrib Miner Petrol 133(1–2):122–135

O'Hara MJ (1995) Trace element geochemical effects of integrated melt extraction and "shaped" melting regimes. J Petrol 36(4):1111–1132

Okino K, Shimakawa Y, Nagaoka S (1994) Evolution of the Shikoku Basin. J Geomagn Geoelectr 46(6):463–479

Ozima M, Kaneoka I, Ujiie H (1977) (super 40) Ar- (super 39) Ar age of rocks, and the development mode of the Philippine Sea. Nature (london) 267(5614):816–818

Pearce JA, Stern RJ, Bloomer SH, Fryer P (2005) Geochemical mapping of the Mariana arc-basin system; implications for the nature and distribution of subduction components. Geochem Geophys Geosyst. https://doi.org/10.1029/2004GC000895

Peccerillo A, Taylor SR (1976) Geochemistry of Eocene calc-alkaline volcanic rocks from the Kastamonu area, northern Turkey. Contrib Mineral Petrol 58(1):63–81

Perfit MR, Gust DA, Bence AE, Arculus RJ, Taylor SR, Le Maitre RW, Cundari A (1980) Chemical characteristics of island-arc basalts; implications for mantle sources. Chem Geol 30(3):227–256

Prowatke S, Klemme S (2006) Trace element partitioning between apatite and silicate melts. Geochim Cosmochim Acta 70(17):4513–4527

Putirka KD (2008) Thermometers and barometers for volcanic systems. Rev Mineral Geochem 69(1):61–120

Putirka K (2016) Amphibole thermometers and barometers for igneous systems and some implications for eruption mechanisms of felsic magmas at arc volcanoes. Am Miner 101(4):841–858

Reagan MK, Ishizuka O, Stern RJ et al (2010) Fore-arc basalts and subduction initiation in the Izu-Bonin-Mariana system. Geochem Geophys Geosyst G3 11(3):Q03X12

Reagan MK, Heaton DE, Schmitz MD, Pearce JA, Shervais JW, Koppers AAP (2019) Forearc ages reveal extensive short-lived and rapid seafloor spreading following subduction initiation. Earth Planet Sci Lett 506:520–529

Ridolfi F, Renzulli A (2012) Calcic amphiboles in calc-alkaline and alkaline magmas; thermobarometric and chemometric empirical equations valid up to 1.130 degrees C and 2.2 GPa. Contrib Mineral Petrol 163(5):877–895

Ronov AB, Yaroshevskiy AA (1976) A new model for the chemical structure of the Earth's crust. Geochem Int 13(6):89–121

Ryan WBF, Carbotte SM, Coplan JO et al (2009) Global Multi-Resolution Topography synthesis. Geochem Geophys Geosyst G3 10(3):Q03014

Samajpati E, Hickey-Vargas R (2020) Geochemistry of volcanic glass from oligocene detrital sediments at DSDP Site 296, Kyushu Palau ridge interpreting the magmatic evolution of the early Northern Izu Bonin Mariana Island Arc. Island Arc https://doi.org/10.1111/iar.12355

Savov IP, Hickey-Vargas R, D'Antonio M, Ryan JG, Spadea P (2006) Petrology and geochemistry of West Philippine Basin basalts and early Palau-Kyushu Arc volcanic clasts from ODP Leg 195, Site

1201D; implications for the early history of the Izu-Bonin-Mariana Arc. J Petrol 47(2):277–299

Schnetzler CC, Philpotts JA (1970) Partition coefficients of rare-earth elements between igneous matrix material and rock-forming mineral phenocrysts; II. Geochim Cosmochim Acta 34(3):331–340

Shaw DM (2000) Continuous (dynamic) melting theory revisited. Can Mineral 38:1041–1063

Shimizu K, Liang Y, Sun C, Jackson CRM, Saal AE (2017) Parameterized lattice strain models for REE partitioning between amphibole and silicate melt. Am Miner 102(11):2254–2267

Sisson TW, Grove TL (1993) Experimental investigations of the role of H_2O in calc-alkaline differentiation and subduction zone magmatism. Contrib Mineral Petrol 113(2):143–166

Smith DJ (2014) Clinopyroxene precursors to amphibole sponge in arc crust. Nat Comm. https://doi.org/10.1038/ncomms5329

Stern RJ, Morris JD, Bloomer SH, Hawkins JW Jr (1991) The source of the subduction component in convergent margin magmas; trace element and radiogenic isotope evidence from Eocene boninites, Mariana Forearc. Geochim Cosmochim Acta 55(5):1467–1481

Stern RJ, Jackson MC, Fryer P, Ito E (1993) O, Sr, Nd and Pb isotopic composition of the Kasuga Cross-Chain in the Mariana Arc; a new perspective on the K-h relationship. Earth Planet Sci Lett 119(4):459–475

Stern RJ, Fouch MJ, Klemperer SL, Eiler JM (2003) An overview of the Izu-Bonin-Mariana subduction factory. Geophys Monograph 138:175–222

Straub SM (2003) The evolution of the Izu Bonin-Mariana volcanic arcs (NW Pacific) in terms of major element chemistry. Geochem Geophys Geosyst G3. https://doi.org/10.1029/2002GC000357

Straub SM (2008) Uniform processes of melt differentiation in the central Izu Bonin volcanic arc (NW Pacific). Geol Soc Special Publications 304:261–283

Sun SS, McDonough WF (1989) Chemical and isotopic systematics of oceanic basalts; implications for mantle composition and processes. Geol Soc Special Publications 42:313–345

Taylor B, Fujioka K, Janecek TR et al (1992) Rifting and the volcanic-tectonic evolution of the Izu-Bonin-Mariana Arc. Proc Ocean Drilling Program Scientific Results 126:627–651

Taylor RN, Nesbitt RW, Smellie JL (1994) Arc volcanism in an extensional regime at the initiation of subduction; a geochemical study of Hahajima, Bonin Islands, Japan. Special Publication - Geol Soc London 81:115–134

Watson EB, Ryerson FJ (1986) Partitioning of zirconium between clinopyroxene and magmatic liquids of intermediate composition. Geochim Cosmochim Acta 50(11):2523–2526

Yamazaki T, Stern RJ (1997) Topography and magnetic vector anomalies in the Mariana Trough. JAMSTEC J Deep Sea Res 13:31–45

Zhang J, Humphreys MCS, Cooper GF, Davidson JP, Macpherson CG (2017) Magma mush chemistry at subduction zones, revealed by new melt major element inversion from calcic amphiboles. Am Mineralogist 10(6):1353–1367